Image reconstruction of multi-channel photoacoustic and laser-ultrasound data using reverse-time migration

Jami L. Johnson[a], Jeffrey Shragge[b], and Kasper van Wijk[a]

[a]The Dodd-Walls Centre for Photonic and Quantum Technologies and Department of Physics, University of Auckland in Auckland, New Zealand;
[b]School of Physics and School of Earth and Environment, University of Western Australia in Perth, Australia

ABSTRACT

We propose a new reconstruction algorithm for photoacoustic and laser-ultrasound imaging based on reverse-time migration (RTM), a time reversal imaging algorithm originally developed for exploration seismology. RTM inherently handles strong velocity heterogeneity and complex propagation paths. A successful RTM analysis with appropriate handling of boundary conditions results in enhanced signal-to-noise, accurately located structures, and minimal artifacts. A laser-ultrasound experiment begins with a source wavefield generated at the surface that propagates through the sample. Acoustic scatterers in the propagation path give rise to a scattered wavefield, which travels to the surface and is recorded by acoustic detectors. To reconstruct the laser-ultrasound image, a synthetic source function is forward propagated and cross-correlated with the time-reversed and back-propagated recorded (scattered) wavefield to image the scatterers at the correct location. Conversely, photoacoustic waves are generated by chromophores within the sample and propagate "one-way" to the detection surface. We utilize the velocity model validated by the laser-ultrasound reconstruction to accurately reconstruct the photoacoustic image with RTM. This approach is first validated with simulations, where inclusions behave both as a photoacoustic source and an acoustic scatterer. Subsequently, we demonstrate the capabilities of RTM with tissue phantom experiments using an all-optical, multi-channel acquisition geometry.

Keywords: photoacoustic imaging, reverse-time migration, laser-ultrasound

1. INTRODUCTION

Photoacoustic (PA) imaging is capable of mapping the optical properties of tissue chromophores up to centimeters deep in tissue.[1] Molecules such as hemoglobin[2] and lipids[3] have distinct optical spectra, thus PA imaging is well suited for many vascular applications. Hydroxyapaitite, the main component of calcification, is not readily detected with conventional PA imaging wavelengths,[3] but has strong acoustic contrast compared to soft tissue. Therefore, it is desirable to combine photoacoustic imaging with complementing modalities, such as ultrasound, for comprehensive imaging of vascular structures.

In this article, we present a dual-modality photoacoustic and laser-ultrasound (LU) system that is sensitive to both optical and acoustic properties of tissues. When optical energy is rapidly absorbed by a tissue chromophore, thermoelastic expansion results,[4] converting the chromophore into a transient acoustic source. Assuming a homogeneous medium, the photoacoustic wave emitted from the source travels directly to the detection surface. A laser-ultrasound source is generated by an analogous photoacoustic effect at the sample surface. The LU wave propagates through the sample and is scattered by structures with contrasting acoustic properties. The goal of PA imaging is to map the initial pressure distribution of the PA source, while LU imaging aims to locate acoustic scattering events. Integrating PA and LU imaging into a hybrid modality provides a more complete profile to diagnose the health of blood vessels.

A multi-channel reflection geometry is used, which incorporates multiple sources for every detector position. To reconstruct the PA and LU images, we use reverse-time migration (RTM), a reconstruction approach originating in the seismic exploration community.[5–7] Conventional RTM propagates waves in all directions by solving the

Further author information: (Send correspondence to J.L.J.)
J.L.J.: E-mail: jami.johnson@auckland.ac.nz, Telephone: +64 (0)9 373 7599 ext 88747

Photons Plus Ultrasound: Imaging and Sensing 2015, edited by Alexander A. Oraevsky, Lihong V. Wang
Proc. of SPIE Vol. 9323, 932314 · © 2015 SPIE · CCC code: 1605-7422/15/$18
doi: 10.1117/12.2077220

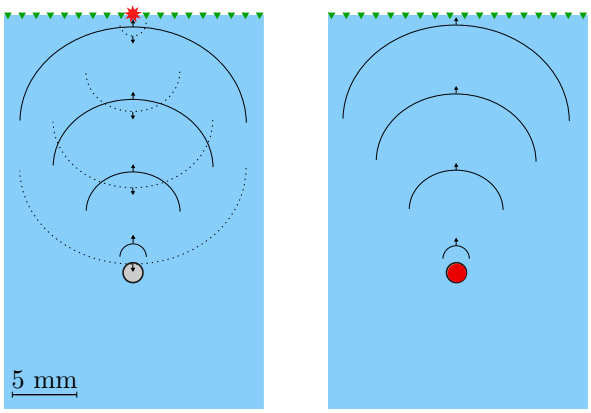

Figure 1. Synthetic model of tube embedded in tissue phantom used for LU (left) and PA (right) simulation with SPECFEM2D. Sources are indicated in red, and detectors are green. In the LU model, the solid line represents the scattered wavefield.

2D (or 3D) acoustic wave equation, therefore it is more robust and accurate than backprojection or time reversal algorithms relying on the one-way wave equation.[8] RTM inherently handles complex velocities and preserves amplitudes,[9] and thus is well suited for photoacoustic and laser-ultrasound reconstruction (PA-RTM, LU-RTM). Velocity errors are more apparent in LU-RTM than for PA-RTM, therefore PA reconstruction is constrained by a velocity model validated with LU-RTM. First, we present results using synthetic PA and LU datasets, followed by validation with a tissue phantom experiment.

2. METHODS

2.1 Synthetic Model

A synthetic model is created using Gmsh meshing software[10] and SPECFEM2D wave propagation software.[11] A second-order quadrilateral mesh simulates a homogeneous acoustic medium with a vessel proxy embedded 2 cm deep. The vessel acts both as a photoacoustic source and an acoustic scatterer, analogous to the experiment described in Sec. 2.2 and detailed in 12.

Figure 1 illustrates the PA and LU models. Surface displacement is recorded by 101 acoustic detectors placed at 200 μm intervals across the surface of the model. LU sources are simulated as 5 MHz first derivative Gaussian wavelets. A reflection configuration is used, with sources placed at 17 equally spaced positions across the 2 cm detection line. For each LU source, the scattered wavefield is recorded at all detectors. A PA source is simulated by 242 evenly distributed point sources inside the vessel, each modeled as a 10 MHz first derivative Gaussian wavelet.

2.2 Phantom Experiment

A solid tissue phantom composed of distilled water, 1% Intralipid (Fresenius Kabi, Uppsala, Sweden), and 1% highly purified agar (A0930-05, U.S. Biological, Swampscott, MA, USA) is constructed to simulate acoustic and optical properties of biological tissues.[13] A 1.4 mm inner diameter acrylic tube filled with infrared absorbing dye (Epolight 2057, Epolin, Newark, NJ, USA) is embedded 2 cm deep. The tube wall (233.5 μm) represents the wall of a blood vessel that is stiffened due to disease, such as calcification. The tube acts as an acoustic scatterer, but is optically transparent. Conversely, the infrared dye is a weak acoustic scatterer, but generates a strong photoacoustic wave by absorption of the source energy (for more details on phantom properties, see 12).

Figure 2 illustrates the experimental setup. An unfocused (8 mm diameter) 1064-nm Nd:YAG source laser with a 10-ns pulse width and 10 Hz repetition rate (Quanta-Ray, Spectra Physics, Newport, Irvine, CA, USA) is used to generate both photoacoustic and laser-ultrasound waves. Acoustic waves are detected using a broadband heterodyne vibrometer (OFV-505, Polytec, Irvine, CA, USA).

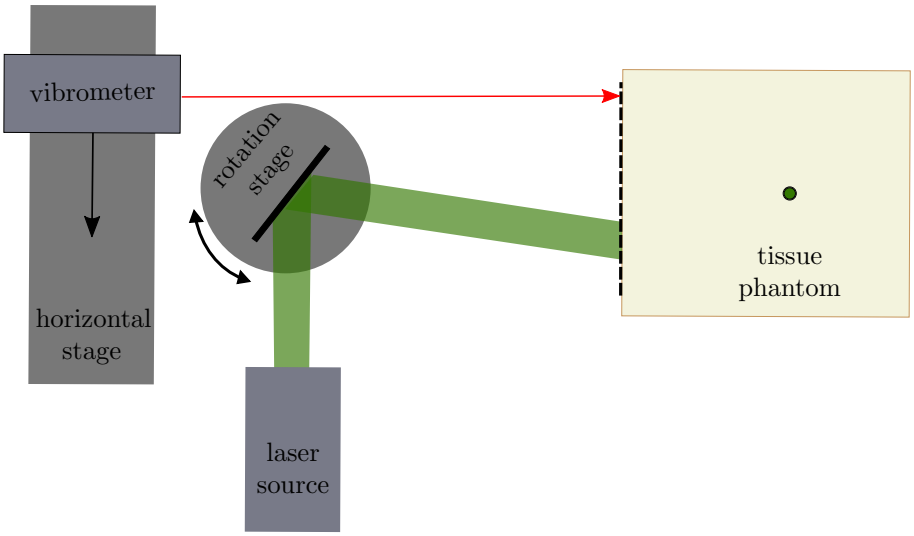

Figure 2. Experimental setup for multi-channel PA and LU acquisition. A pulsed source laser is reflected by a mirror mounted on a rotating stage (URS1000BCC, Newport, Irvine, CA). A heterodyne vibrometer is mounted on a horizontal stage (M-IMS1000LM, Newport). The source laser is stationary while the vibrometer records the wavefield in a line across the phantom surface. The source is then moved incrementally, adjacent to the detection line, with a detection scan performed for each source position.

The vibrometer is scanned across 2 cm of the phantom surface at 200 μm increments. A retroreflective tape (A-RET-T010, Polytec, Irvine, CA, USA) is placed across the detection line to improve the signal strength of the reflected vibrometer probe beam. The source laser is scanned adjacent to the detection line in 1.25 mm increments with a rotating mirror.

A total of 16 shot profiles were recorded: for each source position, the wavefield is recorded at every detector position. First, the laser source is incident on the phantom surface, resulting in high transmission of the optical energy for PA generation and low optical absorption at the phantom surface (Trial 1). Next, the tape is extended across the source line. The tape is partially opaque to infrared wavelengths, resulting in strong LU generation at the surface and attenuation of PA generation (Trial 2). The experiment was fully automated using the open-source PLACE automation package.[14]

2.3 Reconstruction

A straightforward weighted subtraction of Trial 1 from Trial 2 is used to isolate the LU wavefield in Trial 2. In Trial 1, the PA wavefield dominated, therefore both LU and PA wavefields are reconstructed independently.

To reconstruct the LU image, a two-way LU-RTM algorithm is implemented. First, the LU wavefield is simulated by propagating a source function estimate through the model from time $t = 0$ to $t = t_{max}$. This synthetic wavefield is then reversed in time and backpropagated simultaneously with the recorded LU wavefield. To form the image, a zero time lag cross-correlation imaging condition[15] is applied:

$$I(\mathbf{x}) = \sum_{t=0}^{t_{max}} \mathcal{S}(\mathbf{x}, t)\mathcal{R}^{\dagger}(\mathbf{x}, t), \tag{1}$$

where $\mathcal{S}$ is the synthetic source wavefield, $\mathcal{R}$ is the recorded LU wavefield, and † represents an adjoint operator. That is, an image is formed where scattered energy is spatially and temporally co-located in the synthetic source and back-propagated recorded wavefields.

Reflections from the boundary of the computational domain can introduce artifacts when using two-way RTM methods and a cross-correlation imaging condition. To account for this, absorbing[16] or damping[17] boundaries can

be introduced. While effective, these methods tend to be computationally complex, or require propagation in a single direction.[18] Here, we implement a random velocity boundary as outlined in 18. When the source wavefield propagates to the boundary, it is reflected incoherently by the random boundary and is ideally uncorrelated with the recorded LU wavefield. This method efficiently reduces correlations from boundary reflections when a unique random velocity boundary is used for each shot. The resulting images are stacked (summed) to form the final image.

Unlike the LU wavefield, PA waves travel directly from the source (generated at time $t = 0$) to the surface. Therefore, reconstruction is performed by backpropagating only the recorded wavefield, and the wavefield at time $t = 0$ is extracted as the PA image (PA-RTM). The PA source is virtually identical in each shot, except for small frequency variations due to non-uniform optical illumination.[19] Therefore, all shots are stacked into a single wavefield before applying PA-RTM.

3. RESULTS AND DISCUSSION

Reconstructed images for the synthetic and experimental data are shown in Fig. 3 and 4, respectively. For both PA and LU, the use of multi-channel data improves the signal-to-noise when compared with a single shot. In the laser-ultrasound experiments, both the front and back wall are imaged at the correct depth. Stacking multiple shots attenuates reverberations within the tube, as they correlate with the source wavefield at different locations in each shot and do not sum constructively. The sides of the tube are not imaged due to the limited aperture in reflection configuration. Placing sources and detectors around the boundary of the phantom would illuminate these masked areas.

PA-RTM is less sensitive to velocity errors than LU-RTM, such that the wavefield will form a focused image with an inaccurate velocity estimation. However, the image will form at an incorrect location. The redundant acoustic information in the LU and PA data allow us to use the velocity model validated by LU-RTM to constrain the photoacoustic image and ensure accurate PA reconstruction.

Due to the non-uniform distribution of light in tissue,[19] illuminating the target from multiple directions improves PA resolution. Furthermore, stacking all shots before reconstruction suppresses random noise. In both the model and experiment, the sources at the edge of the tube dominate due to high acoustic contrast between the dye and tube wall. Therefore, the wavefield at time $t = 0$ highlights the tube wall. This indicates that the structure of surrounding acoustic scatterers may be recoverable from the PA data.

4. CONCLUSIONS

Photoacoustic and laser-ultrasound images are effectively reconstructed using reverse-time migration of multi-channel data. The velocity model validated by LU-RTM constrains PA-RTM for accurate reconstruction. Improved resolution and signal-to-noise for both synthetic and experimental data was shown with multi-channel acquisition and reconstruction, compared to reconstruction of data with a single source. Furthermore, this work highlights that the PA wavefield contains significant information about surrounding acoustic scatterers.

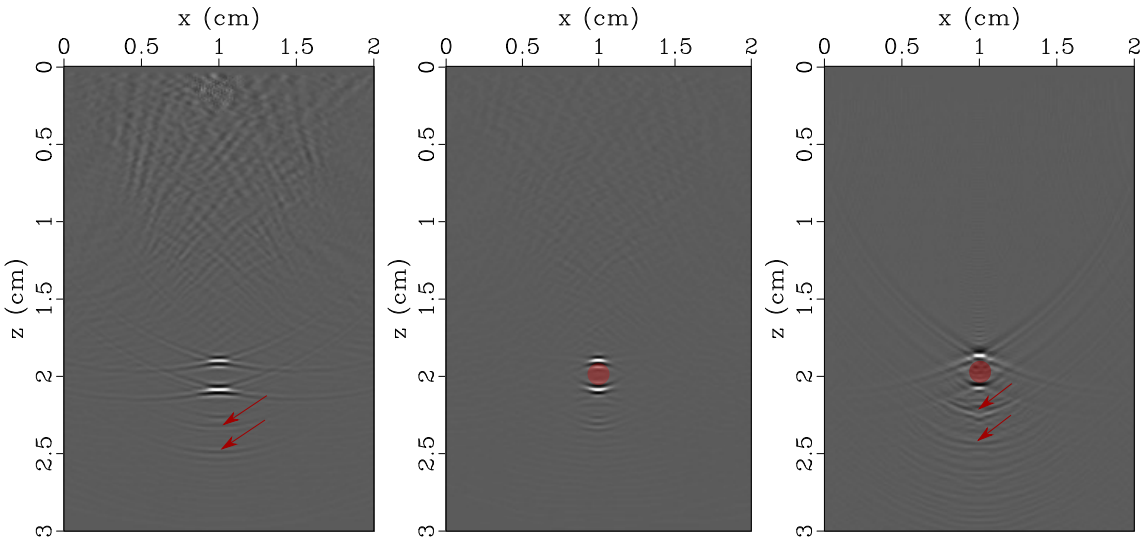

Figure 3. LU-RTM and PA-RTM results using simulated data. Left: LU image using a single source. Red arrows indicate reverberations from the tube wall. Middle: LU image with multiple sources, showing improved resolution and signal-to-noise compared to a single shot. The inner diameter of the tube model is overlayed in red. Right: PA image with inner diameter of tube overlayed. PA generation is strongest near the tube wall. Reverberations are denoted by a red arrow.

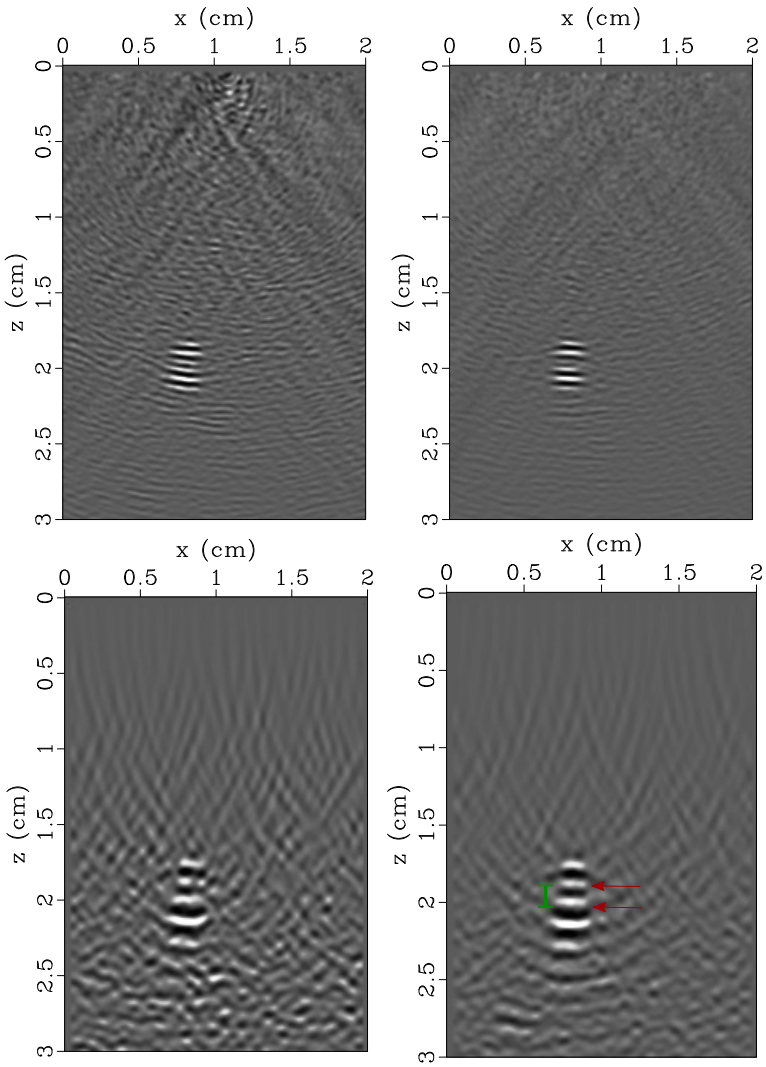

Figure 4. LU-RTM (top panel) and PA-RTM (bottom panel) results for experimental data. The left columns shows reconstruction for one shot (with a single source position). The stacked images are in the right column. Improved resolution and signal to noise are shown for the stacked images. In each image, the tube is imaged at the correct depth. In the stacked PA image, the inner diameter of the tube is indicated in green, and the red arrows denote the location of the tube wall.

REFERENCES

[1] Beard, P., "Biomedical photoacoustic imaging," *Interface Focus* **1**, 602–631 (2011).

[2] Prahl, S., "Optical absorption of hemoglobin," *Oregon Medical Laser Center, http://omlc.ogi.edu/spectra/hemoglobin/index.html* **15** (1999).

[3] Allen, T. J., Hall, A., Dhillon, A. P., Owen, J. S., and Beard, P. C., "Spectroscopic photoacoustic imaging of lipid-rich plaques in the human aorta in the 740 to 1400 nm wavelength range," *J. Biomed. Opt.* **17**(6), 0612091–06120910 (2012).

[4] Wang, B., Karpiouk, A., Yeager, D., Amirian, J., Litovsky, S., Smalling, R., and Emelianov, S., "*In vivo* intravascular ultrasound-guided photoacoustic imaging of lipid in plaques using an animal model of atherosclerosis," *Ultrasound Med. Biol.* **38**(12), 2098–2103 (2012).

[5] Baysal, E., Kosloff, D. D., and Sherwood, J. W., "Reverse time migration," *Geophysics* **48**(11), 1514–1524 (1983).

[6] McMechan, G., "Migration by extrapolation of time-dependent boundary values," *Geophys. Prosp.* **31**(3), 413–420 (1983).

[7] Whitemore, N., "Iterative depth imaging by backward time propagation: 53rd annual international meeting," in [*Soc. Expl. Geophys., Expanded Abstracts*], 382–384 (1983).

[8] Biondi, B., [*3D seismic imaging*], Society of Exploration Geophysicists (2006).

[9] Zhang, Y., Sun, J., and Gray, S., "Reverse-time migration: amplitude and implementation issues," in [*2007 SEG Annual Meeting*], Society of Exploration Geophysicists (2007).

[10] Geuzaine, C. and Remacle, J.-F., "Gmsh: A 3-D finite element mesh generator with built-in pre- and post-processing facilities," *Int. J. Numer. Meth. in Eng.* **79**(11), 1309–1331 (2009).

[11] Cristini, P., Komatitsch, D., Labarta, J., Le Goff, N., Le Loher, P., Martin, R., Morency, C., Peter, D., Tape, C., and Tromp, J., "SPECFEM2D," (2012).

[12] Johnson, J. L., van Wijk, K., and Sabick, M., "Characterizing phantom arteries with multi-channel laser ultrasonics and photo-acoustics," *Ultrasound Med. Biol.* **40**(3), 513–520 (2014).

[13] Cubeddu, R., Pifferi, A., Taroni, P., Torricelli, A., and Valentini, G., "A solid tissue phantom for photon migration studies," *Phys. Med. Biol.* **42**(10), 1971 (1997).

[14] Johnson, J. L., tom Wörden, H., and van Wijk, K., "PLACE: An open-source python package for laboratory automation, control, and experimentation," *J. Lab. Autom.* , 2211068214553022 (2014).

[15] Claerbout, J., [*Imaging the earth's interior*], Blackwell Science Inc, Cambridge (1985).

[16] Sacks, Z. S., Kingsland, D. M., Lee, R., and Lee, J.-F., "A perfectly matched anisotropic absorber for use as an absorbing boundary condition," *IEEE Trans. Antennas Propag.* **43**(12), 1460–1463 (1995).

[17] Cerjan, C., Kosloff, D., Kosloff, R., and Reshef, M., "A nonreflecting boundary condition for discrete acoustic and elastic wave equations," *Geophysics* **50**(4), 705–708 (1985).

[18] Clapp, R. G., "Reverse time migration with random boundaries," in [*79th Annual International Meeting, SEG Expanded Abstracts*], **28**, 2809–2813, Citeseer (2009).

[19] Metwally, M. K., El-Gohary, S. H., Byun, K. M., Han, S. M., Lee, S. Y., Cho, M. H., Khang, G., Cho, J., and Kim, T.-S., "Influence of optical fluence distribution on photoacoustic imaging," *Int. J. Math. Comp. Phys. Quantum Eng.* **8**(8), 0–7 (2014).